Aggressive Flight With Suspended Payloads Using Vision-based Control

Sarah Tang*[1], Valentin Wüest,*[2] and Vijay Kumar[1]
*These authors contributed equally to this manuscript.

***Abstract*—Payload manipulation with aerial robots has been an active research area for many years. Recent approaches have sought to plan, control, and execute maneuvers with large, yet deliberate, load swings for more agile, energy-optimal maneuvering. Unfortunately, the system's nonlinear dynamics make executing such trajectories a significant challenge and experimental demonstrations thus far have relied completely on a motion capture system and non-negligible simplifications like restriction of the system to a two-dimensional workspace or closing of the control loop on the quadrotor, instead of the payload. In this work, we observe the payload using a downward-facing camera and estimate its state relative to the quadrotor using an Extended Kalman Filter. We demonstrate closed-loop payload control in the full three-dimensional workspace, with the planning, estimation, and control pipeline implemented on an onboard processor. We show control of load swings up to 53^o from the vertical axis. To the best of our knowledge, this represents the first realization of closed-loop control of agile slung-load maneuvers and the largest achieved payload angle.**

***Index Terms*—Aerial Systems: Mechanics and Control, Motion Control**

I. Introduction

AUTONOMOUS aerial manipulation can aid in many tasks, such as construction, disaster response, and package delivery. One mechanism for interaction is through a rigidly-connected gripper [1]. However, rigidly attached objects can significantly alter the vehicle's maneuverability and the mostly small size of the gripper requires the robot to approach the ground for pick-up. Instead, we transport objects via a cable suspension, allowing the vehicle to retain its agility.

Past work for slung-load transport has largely focused on elimination of the load swing while maintaining fast vehicular movement [2], [3], [4], [5], [6], [7]. This mode of operation is safe, but conservative and sub-optimal, as the system's natural dynamics, the swinging motions, are suppressed. In contrast, skilled helicopter pilots achieve rapid object transport by allowing payload swings and anticipating their effects[3]. Leveraging the system dynamics like this is not only more energy optimal, but also allows maneuvering around obstacles such as windows shorter than the suspension-cable's length [8]. However, control at configurations where the payload is swung far from the vertical position is challenging. Thus, previous controllers have constrained the system to a planar workspace, completely relied on an external motion capture system, or closed the control loop on the quadrotor, rather than payload position. In this work, we demonstrate closed-loop payload control of aggressive maneuvers and take a significant step towards complete onboard control by detecting the payload's state relative to the quadrotor with a downward-facing camera.

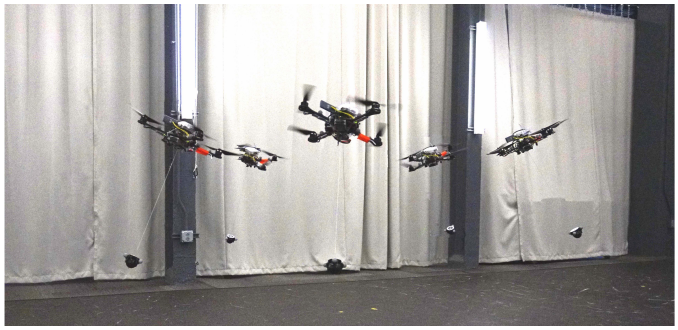

Fig. 1: Snapshots of a quadrotor with suspended payload.

A. Related Work

One approach for aerial slung-load manipulation is to directly optimize system inputs [5], [6], [9]. However, in this work, we will decouple the trajectory generation and control problems. While generating dynamically feasible, aggressive trajectories has already been successfully accomplished using nonlinear optimization [10] or Quadratic Program variants [8], [11], tracking these trajectories is very challenging. Most previous controllers can only stabilize the payload to the vertical position [2], [3], [4], limiting the system to swing-free transport. Only two approaches have addressed executing large load swings. The first explicitly finds the quadrotor trajectory that actuates the desired payload motions and closes the control loop on the robot [10], [11]. However, this is not robust to unmodeled slung-load disturbances, and a more desirable option is to close the control loop on the payload using a geometric controller [12]. Unfortunately, while this

Manuscript received: Sept. 10, 2017; Revised Dec. 12, 2017; Accepted Jan. 1, 2018.

This paper was recommended for publication by Editor Jonathan Roberts upon evaluation of the Associate Editor and Reviewers' comments. We gratefully acknowledge the support of ARL grant W911NF-08-2-0004, NSF grant IIS-1426840, and ARO grant W911NF-13-1-0350. S. Tang is supported by NSF grant DGE-1321851.

[1]S. Tang and V. Kumar are with the General Robotics, Automation, Sensing & Perception (GRASP) Laboratory, University of Pennsylvania, Philadelphia, PA 19104, USA sytang, kumar@seas.upenn.edu

[2]V. Wüest is with the Department of Mechanical Engineering, ETH Zurich, Leonhardstrasse 21, 8092 Zurich, Switzerland vwueest@student.ethz.ch

Digital Object Identifier (DOI): see top of this page.

[3]https://youtu.be/sMVI_os9ioM

controller theoretically guarantees control of arbitrary system orientations with almost global stability, it has not been fully experimentally realized. Previous results restrict the system to a two-dimensional plane [8], [13] or only demonstrate stabilization without validation of agile motions [14].

Earlier implementations have also relied fully on a motion capture system [8], [10], [13], [14]. These measurements do not incorporate information about the system's dynamics and can be especially noisy for small, fast-moving objects like a suspended payload. Filtering onboard sensor measurements with a known dynamic model is thus a more desirable option. This has been done for small payload oscillations about the vertical configuration using force sensors [15] and cameras [3], but has not been demonstrated with large load swings.

B. Contribution

The main contribution of this work is a vision-based, closed-loop geometric controller that enables the control of a suspended payload by a quadrotor even at large displacements. Our estimation and control algorithms rely on state representations that do not suffer from singularities. Furthermore, these algorithms can be run on a low-cost processor. We show that our system can execute aggressive maneuvers and offers notable performance gain over closing the control loop on the quadrotor (i.e. open-loop payload control). While the aggressive control of quadrotors has been well-addressed, this is the first demonstration of closed-loop control of suspended payloads with load swings exceeding 50^o.

We note that the focus of this work is on estimation of the payload state relative to the robot. Others have shown that onboard cameras can be used for quadrotor state estimation [16], [17]. In this work, we use a motion capture system to measure the quadrotor position, velocity, and yaw, but this can naturally be replaced with existing quadrotor estimation techniques.

Sections II–III will present the dynamic model and control design. Section IV and V will describe the estimator and trajectory generator. Section VI will present experimental results and finally, Section VII will conclude the paper.

II. Modeling

We model the payload as a point-mass and the cable as a massless rod. Let $\mathcal{I}$ be an inertial coordinate frame, with axes $\{\mathbf{e}_x^{\mathcal{I}}, \mathbf{e}_y^{\mathcal{I}}, \mathbf{e}_z^{\mathcal{I}}\}$, $\mathcal{B}$ be a body frame with axes $\mathbf{e}_*^{\mathcal{B}}$, and $\mathcal{C}$ be a camera frame with axes $\mathbf{e}_*^{\mathcal{C}}$. Fig. 2 illustrates these frames and Table I lists relevant variables. The state and input are:

$$\mathbf{x} = \begin{bmatrix}\mathbf{x}_L^\top & \dot{\mathbf{x}}_L^\top & \mathbf{p}^\top & \dot{\mathbf{p}}^\top & \mathbf{R} & \mathbf{\Omega}^\top\end{bmatrix}^\top,$$
$$\mathbf{u} = \begin{bmatrix} f & \mathbf{M}^\top\end{bmatrix}^\top,$$

respectively. $\mathbf{p}$ and $\mathbf{R}$ are coordinate-free configuration representations that avoid parameterization singularities. The system's kinetic and potential energy is:

$$\begin{aligned}\mathcal{T} =& \tfrac{1}{2}(m_Q + m_L)\dot{\mathbf{x}}_L \cdot \dot{\mathbf{x}}_L - m_Q l\ \dot{\mathbf{x}}_L \cdot \dot{\mathbf{p}} \\ &+ \tfrac{1}{2}\ m_Q l^2 \dot{\mathbf{p}} \cdot \dot{\mathbf{p}} + \tfrac{1}{2}\ \mathbf{\Omega}\ \mathbb{I}\ \mathbf{\Omega}, \\ \mathcal{U} =& (m_Q + m_L) g\ \mathbf{x}_L \cdot \mathbf{e}_z^{\mathcal{I}} - m_Q g l\ \mathbf{p} \cdot \mathbf{e}_3,\end{aligned}$$

TABLE I: Variables of the quadrotor-with-load system.

$\mathcal{I}, \mathcal{B}, \mathcal{C}$	Inertial, body, camera frame
$l, d \in \mathbb{R}$	Cable length, distance from camera to load
$m_Q, m_L; g \in \mathbb{R}$	Mass of quad, load; gravity constant
$\mathbb{I} \in \mathbb{R}^{3,3}$	Inertia tensor of quad, in $\mathcal{B}$
$f \in \mathbb{R}$, $\mathbf{M} \in \mathbb{R}^3$	Input thrust magnitude, moment in $\mathcal{B}$
$\mathbf{x}_Q, \mathbf{x}_L \in \mathbb{R}^3$	Position vector of quad, load, in $\mathcal{I}$
$\mathbf{p} \in \mathbb{S}^2$	Unit vector from quad to load, in $\mathcal{I}$
$\mathbf{R} \in SO(3), \psi \in \mathbb{R}$	Rotation from $\mathcal{B}$ to $\mathcal{I}$, yaw angle of quad
$\mathbf{\Omega} \in \mathbb{R}^3$	Angular velocity of quad, in $\mathcal{B}$

respectively. The virtual work of the system is given by:

$$\delta\mathcal{W} = f\boldsymbol{R}\mathbf{e}_z^{\mathcal{I}} \cdot (\delta\mathbf{x}_L - l\delta\mathbf{p}) + \mathbf{M} \cdot (\boldsymbol{R}^\top \delta\boldsymbol{R}).$$

The variation $\delta\mathbf{x}_L$ exists in $\mathbb{R}^3$, however, the other variational terms must be defined on their respective manifolds:

$$\delta\mathbf{p} = \hat{\boldsymbol{\xi}}\mathbf{p} \in T\mathbb{S}^2, \boldsymbol{\xi} \in \mathbb{R}^3, \text{ where } \boldsymbol{\xi} \cdot \mathbf{p} = 0,$$
$$\delta\mathbf{R} = \mathbf{R}\hat{\boldsymbol{\eta}} \in TSO(3), \boldsymbol{\eta} \in \mathbb{R}^3.$$

The hat map, $\hat{\cdot}$, returns the skew-symmetric matrix such that $\hat{\mathbf{x}}\mathbf{y} = \mathbf{x} \times \mathbf{y}$. $\delta\dot{\mathbf{x}}_L, \delta\dot{\mathbf{p}}, \delta\mathbf{\Omega}$ can be found by differentiation. Using these values in the Lagrange d'Alembert principle:

$$\delta S = \int_{t_1}^{t_2} (\delta W + \delta\mathcal{T} - \delta\mathcal{U}) dt = 0,$$

and integrating by parts gives the system dynamics:

$$\begin{aligned}\tfrac{d}{dt}\mathbf{x}_L &= \dot{\mathbf{x}}_L, \\ (m_Q{+}m_L)(\ddot{\mathbf{x}}_L{+}g\mathbf{e}_z^{\mathcal{I}}) &= \left(\mathbf{p} \cdot f\mathbf{R}\mathbf{e}_z^{\mathcal{I}} - m_Q l\left(\dot{\mathbf{p}} \cdot \dot{\mathbf{p}}\right)\right)\mathbf{p}, \\ \tfrac{d}{dt}\mathbf{p} &= \dot{\mathbf{p}}, \\ m_Q l\left(\ddot{\mathbf{p}} + \left(\dot{\mathbf{p}} \cdot \dot{\mathbf{p}}\right)\mathbf{p}\right) &= \mathbf{p} \times \left(\mathbf{p} \times f\mathbf{R}\mathbf{e}_z^{\mathcal{I}}\right), \\ \dot{\mathbf{R}} &= \mathbf{R}\ \hat{\mathbf{\Omega}}, \\ \dot{\mathbf{\Omega}} &= \mathbb{I}^{-1}\left(\mathbf{M} - \mathbf{\Omega} \times \mathbb{I}\ \mathbf{\Omega}\right).\end{aligned}$$

Details of this calculation can be found in [12].

A key observation is that the system is differentially flat [18], that is, all state and input variables can be expressed as nonlinear equations of a set of flat variables and their derivatives. In this case, the flat variables are [12]:

$$\mathbf{x}_f = \begin{bmatrix}\mathbf{x}_L^\top & \psi\end{bmatrix}^\top.$$

To see this, begin with the Newton-Euler equation:

$$-T\mathbf{p} = m_L(\ddot{\mathbf{x}}_L + g\mathbf{e}_z^{\mathcal{I}}), \tag{1}$$

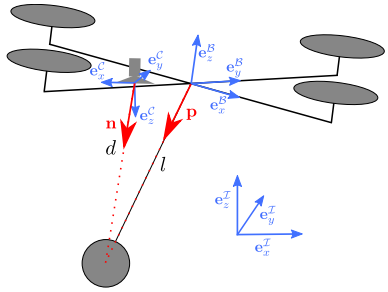

Fig. 2: The quadrotor, payload, and onboard camera with the inertial, body, and camera frames.

where T represents the magnitude of the cable tension. Then:

$$\mathbf{p} = -\frac{(\ddot{\mathbf{x}}_L + g\mathbf{e}_z^{\mathcal{I}})}{\|\ddot{\mathbf{x}}_L + g\mathbf{e}_z^{\mathcal{I}}\|_2}, \tag{2}$$

$\dot{\mathbf{p}}$ can be found through differentiation of Eq. 2. The quadrotor's position and higher derivatives can then be found using:

$$\mathbf{x}_Q = \mathbf{x}_L - l\mathbf{p}. \tag{3}$$

The quadrotor is a differentially-flat system with flat variables $\begin{bmatrix}\mathbf{x}_Q^\top & \psi\end{bmatrix}^\top$ [19], so the rotational states and input can be derived. The highest derivatives of $\mathbf{x}_L$, ψ needed to recover $\mathbf{x}$ and $\mathbf{u}$ are $\mathbf{x}_L^{(6)}$,$\ddot{\psi}$, respectively. For the remainder of this work, assume ψ is constant. Furthermore, assume the cable remains taut (i.e. $T > 0$). From Eq. 1, this is ensured for $\|\ddot{\mathbf{x}}_L + g\mathbf{e}_z^{\mathcal{I}}\|_2 > 0$, which we will guarantee during planning.

III. Control

Crucial to the system is a controller that can track aggressive trajectories. Note state variables are expressed in frames listed in Table I. Subscripts des will denote values planned by the trajectory generator, while c will denote commanded values calculated within the controller.

Differential flatness guarantees that any six-times differentiable trajectory $\mathbf{x}_{L,des}$ can be mapped to dynamically feasible states and inputs, $\mathbf{x}_{des}$ and $\mathbf{u}_{des}$. This motivates a trajectory generator that directly optimizes $\mathbf{x}_{L,des}$, as shown in Section V, and a hierarchical controller, pictured in Fig. 3. The desired trajectory is passed to an outermost payload position controller, which determines a desired payload orientation and angular velocity. This is tracked by a payload attitude controller, which calculates a desired quadrotor orientation, angular velocity, and thrust vector. The innermost quadrotor attitude controller calculates inputs $f, \mathbf{M}$. To execute large load swings, the controller must not depend on local linearizations or be defined by attitude parameterizations that contain singularities. The geometric controller from [12], described below, uniquely displays these properties.

The quadrotor attitude controller is defined with:

$$\begin{aligned}\mathbf{M} =& -\mathbf{k}_R\mathbf{e}_R - \mathbf{k}_\Omega\mathbf{e}_\Omega \\ &+ \boldsymbol{\Omega}\times\mathbb{I}\boldsymbol{\Omega} - \mathbb{I}\left(\hat{\Omega}\times\mathbf{R}^\top\mathbf{R}_c\boldsymbol{\Omega}_{\boldsymbol{c}} - \mathbf{R}^\top\mathbf{R}_c\dot{\boldsymbol{\Omega}}_c\right),\end{aligned}$$

with error functions:

$$\mathbf{e}_R = \tfrac{1}{2}\left(\mathbf{R}_c^\top\mathbf{R} - \mathbf{R}^\top\mathbf{R}_c\right)^\vee,\ \mathbf{e}_\Omega = \boldsymbol{\Omega} - \mathbf{R}^\top\mathbf{R}_c\boldsymbol{\Omega}_c,$$

where $(\cdot)^\vee$ is the inverse of the hat map and $\mathbf{k}_R, \mathbf{k}_\Omega$ are diagonal gain matrices. Unlike a linearized controller, the error functions are defined on the manifold $TSO(3)$. For positive-definite gain matrices and initial conditions where the angle-axis rotation from $\mathbf{R}$ to $\mathbf{R}_c$ has angle less than 180^o, the closed-loop quadrotor attitude error dynamics are exponentially stable about $(\mathbf{e}_R, \mathbf{e}_\Omega) = \mathbf{0}$ [12], [20].

$\mathbf{R}_c, \boldsymbol{\Omega}_c$, are obtained from the payload attitude controller:

$$\begin{aligned}\mathbf{F} =& m_Q l\left(-k_p\mathbf{e}_p - k_{\dot{p}}\mathbf{e}_{\dot{p}} + \left(\mathbf{p}\cdot(\mathbf{p}_c\times\dot{\mathbf{p}}_c)\right)(\mathbf{p}\times\dot{\mathbf{p}})\right. \\ &\left.+ (\mathbf{p}_c\times\ddot{\mathbf{p}}_c)\times\mathbf{p}\right) - (\mathbf{p}_c\cdot\mathbf{p})\mathbf{p}_c.\end{aligned} \tag{4}$$

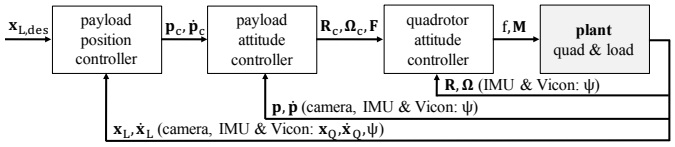

Fig. 3: Controller structure and sensor feedback.

$\mathbf{F}$ is defined with error functions:

$$\mathbf{e}_p = \hat{\mathbf{p}}^2\mathbf{p}_c, \quad \mathbf{e}_{\dot{p}} = \dot{\mathbf{p}} - (\mathbf{p}_c\times\dot{\mathbf{p}}_c)\times\mathbf{p}.$$

Again, $\mathbf{e}_p, \mathbf{e}_{\dot{p}}$ are defined directly on the manifold $T\mathbb{S}^2$. From Eq. 4, the thrust input can be found as:

$$f = \mathbf{F}\cdot\mathbf{R}\mathbf{e}_z^{\mathcal{I}}.$$

The commanded orientation is found as:

$$\mathbf{R}_c = \begin{bmatrix}\frac{\mathbf{b}_{3c}\times\mathbf{c}_{1c}}{\|\mathbf{b}_{3c}\times\mathbf{c}_{1c}\|_2}\times\mathbf{b}_{3c} & \frac{\mathbf{b}_{3c}\times\mathbf{c}_{1c}}{\|\mathbf{b}_{3c}\times\mathbf{c}_{1c}\|_2} & \mathbf{b}_{3c}\end{bmatrix}, \hat{\Omega}_c = \boldsymbol{R}_c^\top\dot{\boldsymbol{R}}_c, \tag{5}$$

where:

$$\mathbf{b}_{3c} = \frac{\mathbf{F}}{\|\mathbf{F}\|_2},\ \mathbf{c}_{1c} = \begin{bmatrix}\cos(\psi) & \sin(\psi) & 0\end{bmatrix}^\top.$$

$\dot{\mathbf{R}}_c$ and $\dot{\boldsymbol{\Omega}}_c$ can be found by differentiating Eq. 5. For positive gains $k_p, k_{\dot{p}}$ and initial angles less than 180^o between $\mathbf{p}$ and $\mathbf{p}_c$, the state $(\mathbf{e}_p, \mathbf{e}_{\dot{p}}, \mathbf{e}_R, \mathbf{e}_\Omega) = \mathbf{0}$ is an exponentially stable equilibrium of the closed-loop error dynamics [12].

Finally, the payload position controller is:

$$\begin{aligned}\mathbf{A} =& (m_Q + m_L)\big(-\mathbf{k}_x\mathbf{e}_{x_L} - \mathbf{k}_v\mathbf{e}_{\dot{x}_L} - \mathbf{k}_i - \int\mathbf{e}_{x_L}dt\big) \\ &+ (m_Q + m_L)(\ddot{\mathbf{x}}_L + g\mathbf{e}_z^{\mathcal{I}}) + m_Q l(\dot{\mathbf{p}}\cdot\dot{\mathbf{p}})\mathbf{p},\end{aligned}$$

where $\mathbf{k}_x, \mathbf{k}_v, \mathbf{k}_i$ are diagonal gain matrices, $\mathbf{e}_{x_L} = \mathbf{x}_L - \mathbf{x}_{L,des}$, and $\mathbf{e}_{\dot{x}_L} = \dot{\mathbf{x}}_L - \dot{\mathbf{x}}_{L,des}$. This defines a commanded payload orientation:

$$\mathbf{p}_c = -\frac{\mathbf{A}}{\|\mathbf{A}\|_2}.$$

$\dot{\mathbf{p}}_c$ can again be found through direct differentiation. For positive-definite $\mathbf{k}_x, \mathbf{k}_v, \mathbf{k}_i$ and initial payload and quadrotor attitude errors satisfying the previously stated bounds, the complete closed-loop error dynamics are exponentially attractive about $(\mathbf{e}_x, \mathbf{e}_y, \mathbf{e}_p, \mathbf{e}_{\dot{p}}, \mathbf{e}_R, \mathbf{e}_\Omega) = \mathbf{0}$ [12].

The controller is defined in a coordinate-free manner, does not require linearization of the system dynamics, and is exponentially attractive in almost all of $\mathbb{R}^3\times TSO(3)\times T\mathbb{S}^2$, and thus well-suited to track aggressive trajectories.

IV. Payload Estimation

The controller requires accurate payload state measurements. We detect the load using a downward-facing camera and filter measurements using an Extended Kalman Filter (EKF), yielding high-frequency, dynamics-informed estimates. Variables, unless otherwise specified, are stated in Table I.

Fig. 3 illustrates sensor feedback for each control loop. Our robot is equipped with a downward-facing fisheye lens camera and an Inertial Measurement Unit (IMU). We obtain the

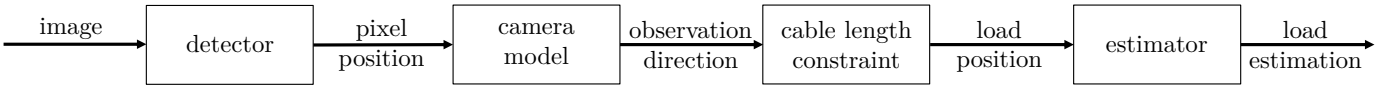

Fig. 4: Flow diagram of the payload estimation pipeline.

quadrotor's roll, pitch, and $\mathbf{\Omega}$ from filtered IMU measurements from native software on the AscTec Hummingbird[4]. Because the yaw ψ is not observable at hover, we obtain ψ from a Vicon[5] motion capture system. For the payload attitude control loop, we design an EKF to fuse IMU and Vicon yaw measurements with images from the onboard camera to estimate $\mathbf{p}, \dot{\mathbf{p}}$. Finally, we combine these estimates with Vicon measurements of $\mathbf{x}_Q, \dot{\mathbf{x}}_Q$ using Eq. 3 to implement the payload position control loop. In future work, our method can be fused with many existing visual or visual-inertial quadrotor estimation techniques. For the quadrotor attitude control loop, we use only IMU and Vicon yaw measurements.

This section will focus on the estimation of $\mathbf{p}$ and $\dot{\mathbf{p}}$. Fig. 4 shows the pipeline, with each step described below.

A. Detector

We detect the payload via an attached black and white circular tag (Fig. 5a). We obtain the tag's pixel position, $\mathbf{x}_u = [u, v]^\top$, in each image from an open-source detector [21]. This system has sub-pixel precision, is robust to variable lighting conditions, and requires relatively little processing time

B. Camera Model

We model the camera with an omnidirectional model [22]. An affine transformation between the tag center in pixel coordinates, $\mathbf{x}_u = [u, v]^\top$, and adjusted pixel coordinates, $\mathbf{x}_{u'} = [u', v']^\top$, accounting for lens-sensor misalignments. The vector from the camera to payload, in the camera frame, is:

$$\mathbf{n}^{\mathcal{C}} = \begin{bmatrix} n_x \\ n_y \\ n_z \end{bmatrix} \approx \lambda \begin{bmatrix} u' \\ v' \\ f(u', v') \end{bmatrix},$$

where the factor λ accounts for the scale ambiguity. The imaging function $f(u', v')$ is approximated with a Taylor series expansion. Assuming the lens is rotationally symmetric, we define $\rho := \sqrt{u'^2 + v'^2}$ and express the Taylor series as:

$$f(u', v') = f(\rho) = a_0 + a_1\rho + a_2\rho^2 + \ldots + a_N\rho^N, \quad (6)$$

where N is tuned. The affine transformation and $a_0, \ldots, a_N$ are found during calibration. This allows us to obtain $\mathbf{n}^{\mathcal{C}}$.

C. Cable Length Constraint

From Fig. 2, we see under the cable-taut assumption that:

$$\mathbf{x}_L^{\mathcal{B}} = l\ \mathbf{p}^{\mathcal{B}} = \mathbf{x}_C^{\mathcal{B}} + d\ \mathbf{R}_{\mathcal{C}}^{\mathcal{B}}\ \mathbf{n}^{\mathcal{C}}. \quad (7)$$

$\mathbf{x}_L^{\mathcal{B}}$ is payload's position and $\mathbf{x}_{\mathcal{C}}^{\mathcal{B}}$ is the camera's position, both in the body frame. $\mathbf{R}_C^{\mathcal{B}}$ is the camera-to-body-frame rotation matrix. Also, note that $\mathbf{x}_{\mathcal{C}}^{\mathcal{B}}$ is known. We formulate:

$$l = \left| \mathbf{x}_C^{\mathcal{B}} + d\ \mathbf{n}^{\mathcal{B}} \right|,$$

and solve for d. We select the solution corresponding to the load oriented below the quadrotor. We then use Eq. 7 to find $\mathbf{x}_L^{\mathcal{B}}$, the position of the payload relative to the quadrotor.

D. Model-based Estimator

For estimation, we consider a system with state:

$$\mathbf{X} = \begin{bmatrix} \mathbf{p}^\top & \dot{\mathbf{p}}^\top \end{bmatrix}^\top,$$

where $\mathbf{p}, \dot{\mathbf{p}}$ are in $\mathcal{I}$, with input:

$$\mathbf{U} = \begin{bmatrix} f & \boldsymbol{R} & \mathbf{\Omega}^\top \end{bmatrix}^\top.$$

Here, f is calculated by the controller while $\mathbf{R}$ and $\mathbf{\Omega}$ are obtained from IMU and Vicon yaw measurements.

We model the process noise as additive Gaussian white noise $\mathbf{N} \in \mathbb{R}^6$ with zero mean and standard deviation $\mathbf{Q} \in \mathbb{R}^{6,6}$. The resulting process model is:

$$\begin{aligned} \dot{\mathbf{X}} &= \begin{bmatrix} \dot{\mathbf{p}} \\ \ddot{\mathbf{p}} \end{bmatrix} = \mathbf{f}(\mathbf{X}, \mathbf{U}, \mathbf{N}), \qquad \mathbf{N} \sim \mathcal{N}(0, \mathbf{Q}), \\ &= \begin{bmatrix} \dot{\mathbf{p}} \\ \frac{1}{m_Q l}\mathbf{p} \times (\mathbf{p} \times f\mathbf{R}\mathbf{e_3}) - (\dot{\mathbf{p}} \cdot \dot{\mathbf{p}})\mathbf{p} \end{bmatrix} + \mathbf{N}. \end{aligned} \quad (8)$$

We obtain $\mathbf{x}_L^{\mathcal{B}}$ from Sections IV-A – IV-C and calculate a numerical discrete time derivative for $\dot{\mathbf{x}}_L^{\mathcal{B}}$. The measurement model, with additive Gaussian white noise $\mathbf{V} \in \mathbb{R}^6$ with zero mean and standard deviation $\mathbf{S} \in \mathbb{R}^{6,6}$, is:

$$\begin{aligned} \mathbf{Z} &= \begin{bmatrix} \mathbf{x}_L^{\mathcal{B}} \\ \dot{\mathbf{x}}_L^{\mathcal{B}} \end{bmatrix} = \mathbf{g}(\mathbf{X}, \mathbf{U}, \mathbf{V}), \qquad \mathbf{V} \sim \mathcal{N}(0, \mathbf{S}), \\ &= \begin{bmatrix} \mathbf{R}^\top l\ \mathbf{p} \\ l\left(\mathbf{R}^\top \dot{\mathbf{p}} - \mathbf{\Omega} \times \left(\mathbf{R}^\top \mathbf{p}\right)\right) \end{bmatrix} + \mathbf{V}. \end{aligned} \quad (9)$$

We use Eqs. 8 and 9 in a standard EKF implementation [23]. Note we also formulate the EKF in a coordinate-free manner. While camera measurements are low-frequency, the EKF uses the dynamic model to estimate the state at the higher IMU measurement rate. We conduct a process update when a new IMU measurement is received, using the most recent control input and yaw measurement. When a new raw image is received, we cache the current state estimate, the subsequent IMU and Vicon measurements, and control inputs. After $\mathbf{x}_L^{\mathcal{B}}, \dot{\mathbf{x}}_L^{\mathcal{B}}$ are computed, we conduct the measurement update on the first state estimate cached and recompute the process updates, accounting for image processing latency.

V. Trajectory Generation

We plan trajectories for the system by optimizing a payload trajectory $\mathbf{x}_{L,des} \in \mathbb{R}^3$. For dynamic feasibility, the trajectory must be at least six-times differentiable and of class $\mathcal{C}^5$. From Section II, the highest derivative to appear in the input is $\mathbf{x}_L^{(6)}$, motivating the cost functional:

$$\mathbf{x}_{L,des} = \arg\min_{\mathbf{x}_L} \int_0^{t_m} \|\mathbf{x}_L^{(6)}\|_2^2\ dt. \quad (10)$$

[4]www.asctec.de
[5]www.vicon.com

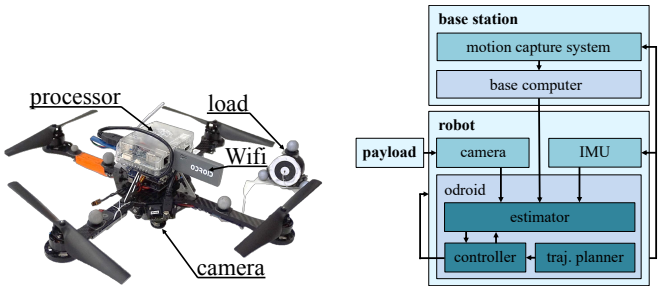

(a) Hardware components. (b) Experimental architecture.

Fig. 5: Overview of experimental setup.

The Euler-Lagrange condition yields the condition:

$$\mathbf{x}_L^{(12)} = 0, \tag{11}$$

whose solution is an 11^{th}-order polynomial. Thus, optimal payload trajectories take the form of piecewise-polynomials:

$$\mathbf{x}_{L,des} = \begin{cases} \mathbf{x}_{L,des,1} = \sum_{i=0}^{11} c_{i,0} t^i & t_0 \leq t \leq t_1 \\ \mathbf{x}_{L,des,2} = \sum_{i=0}^{11} c_{i,1} t^i & t_1 < t \leq t_2 \\ \ldots \\ \mathbf{x}_{L,des,m} = \sum_{i=0}^{11} c_{i,m-1} t^i & t_{m-1} < t \leq t_m, \end{cases}$$

where $\mathcal{T} = \{t_0, ..., t_m\}$ is a pre-selected set of breaktimes and $\mathbf{x}_{L,des}$ is a vector function. Consider the decision vector:

$$\mathbf{c} = \begin{bmatrix} c_{0,0} & c_{1,0} & c_{2,0} & \ldots & c_{N,m-1} \end{bmatrix}^\top.$$

Eq. 10 is a positive-definite quadratic function with respect to $\mathbf{c}$. For dynamic feasibility, we impose continuity constraints:

$$\mathbf{x}_{L,des,j}^{(k)}(t_j) = \mathbf{x}_{L,des,j+1}^{(k)}(t_j) \ \forall j \in [0,5], k \in [1, m\text{-}1]. \tag{12}$$

To ensure the system begins and ends at hover, we impose:

$$\mathbf{x}_{L,des}^{(k)}(t_j) = \mathbf{0} \ \forall j \in \{0, m\}, k \in [1,5]. \tag{13}$$

Note that the flat derivatives in Eq. 13 correspond to states $\mathbf{p} = -\mathbf{e}_z^{\mathcal{I}}$, $\mathbf{R} = \mathcal{I}$, $\dot{\mathbf{p}} = \boldsymbol{\Omega} = \mathbf{0}$. Finally, we select waypoints $\mathbf{x}_{L,j}$ for the trajectory to pass through and impose:

$$\mathbf{x}_{L,des}(t_j) = \mathbf{x}_{L,j} \ \forall j \in [0, m]. \tag{14}$$

Eqs. 12–14 are linear with respect to $\mathbf{c}$. Using Eq. 10 and Eqs. 12–14, we formulate a Quadratic Program (QP) that can be solved with commercial optimization software [8], [19].

There is a possibility that the optimized trajectory $\mathbf{x}_{L,des}$ violates the cable-tautness assumptions of our system. From Eq. 1, guaranteeing $\ddot{\mathbf{x}}_L \cdot \mathbf{e}_z > -g$ is sufficient to ensure $T > 0$. It has been shown that for any $\mathbf{x}_{L,des}$ with breaktimes $\mathcal{T}$, a trajectory with the same coefficients but breaktimes $\alpha\mathcal{T}$ traverses the same path and has derivatives $\frac{\mathbf{x}_{L,des}^{(k)}}{\alpha^k}$ [19]. To ensure cable-tautness, we first find the desired trajectory coefficients by solving the QP with an initial $\mathcal{T}$. We then find the trajectory breaktimes by choosing α such that $\ddot{\mathbf{x}}_L \cdot \mathbf{e}_z > -g$.

VI. Experimental Results

This section presents experimental results that validate our proposed system. A video of the experiments can be found at https://youtu.be/LKss_zhXShU.

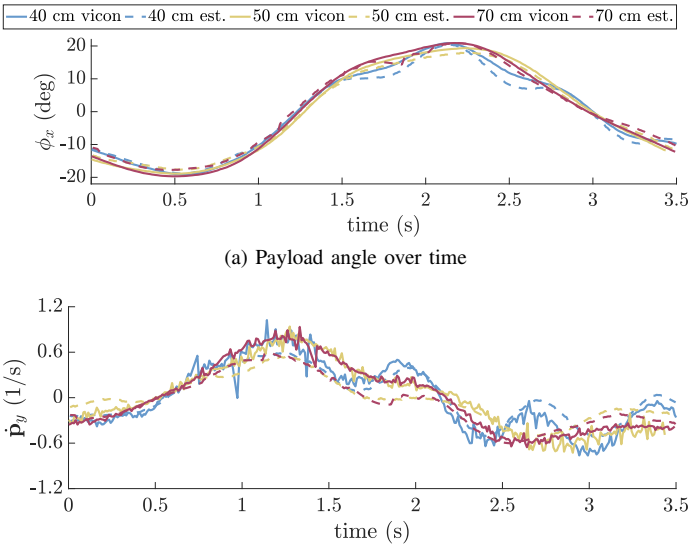

(a) Payload angle over time

(b) $\dot{\mathbf{p}}_y$ over time

Fig. 6: Circle tracking with $T = 3.5$ s at various l.

A. Platform

Fig. 5a pictures our experimental platform. We use an AscTec Hummingbird with an onboard ODROID XU4 processor[6]. The robot has a total mass of 835 g, the payload has a mass of 88 g, and the cable length varies from $0.4 - 0.7$ m.

Our system architecture is shown in Fig. 5b. A base station computer receives the quadrotor states from the Vicon system at 100 Hz and broadcasts them over Wifi to the ODROID. The payload is observed using a MLC200w Matrix-Vision[7] Bluefox camera with a Sunex DSL215 fisheye lens. The ODROID receives images from the camera via USB at 50 Hz and orientation information from the IMU via serial connection at 100 Hz. The innermost quadrotor attitude controller is run onboard a low-level micro-controller on the robot. All other software was implemented in C++/ROS on the ODROID, with Gurobi[8] as an optimization solver.

As suggested by [24], we calibrate the camera using $N = 4$ in Eq. 6. We use control gains $\mathbf{k}_x = \text{diag}(2.9, 2.9, 6.5)$, $\mathbf{k}_v = \text{diag}(1.3, 1.3, 4.5)$, $\mathbf{k}_i = \text{diag}(0.001, 0.001, 0.001)$, $k_p = 9$, $k_{\dot{p}} = 7.5$,

[6]www.hardkernel.com
[7]www.matrix-vision.com/home-en.html
[8]www.gurobi.com

TABLE II: Estimation error statistics for circle trajectories.

l	Statistic	$T = 3.5$ s	$T = 5$ s	$T = 9$ s
$l = 40$cm	Ang. err. mean (deg)	1.60	1.53	1.39
	Ang. std. dev. (deg)	0.74	0.90	0.55
	$\dot{\mathbf{p}}$ err. mean (1/s)	0.11	0.098	0.074
	$\dot{\mathbf{p}}$ std. dev. (1/s)	0.086	0.083	0.050
$l = 50$cm	Ang. err. mean (deg)	1.32	0.86	1.18
	Ang. std. dev. (deg)	0.68	0.38	0.77
	$\dot{\mathbf{p}}$ err. mean (1/s)	0.15	0.081	1.12
	$\dot{\mathbf{p}}$ std. dev. (1/s)	0.11	0.057	0.090
$l = 70$cm	Ang. err. mean (deg)	1.14	1.48	0.73
	Ang. std. dev. (deg)	0.67	0.77	0.44
	$\dot{\mathbf{p}}$ err. mean (1/s)	0.10	0.088	0.051
	$\dot{\mathbf{p}}$ std. dev. (1/s)	0.061	0.057	0.036

Fig. 7: Snapshots of quadrotor moving through a slalom course.

$\mathbf{k}_R = \text{diag}(1.4, 1.4, 0.4)$, $\mathbf{k}_\Omega = \text{diag}(0.12, 0.12, 0.04)$. Here, $\text{diag}(\cdot,\cdot,\cdot)$ specifies the matrix's diagonal elements.

B. Robustness to Varying Parameters

First, we test our system by executing circular trajectories:

$$\mathbf{x}_{L,des} = [r\cos(\frac{2\pi t}{T}) \quad r\sin(\frac{2\pi t}{T}) \quad H]^\top,$$

with cable lengths 40 cm, 50 cm, 70 cm and trajectory periods T of 9 s, 5 s, and 3.5 s. All trajectories have constant altitudes H, $r = 1.5$ m, and are executed for $4T$ s. Across experiments, the payload path remains constant, while the payload and quadrotor orientations and velocities, as well as the quadrotor path, vary. Payload detection and control both become more difficult as T decreases. As l increases, the payload becomes harder to detect, but easier to control. Thus, we can gain an understanding of system robustness through testing combinations of l and T.

Let $\cdot_x, \cdot_y, \cdot_z$ denote vector components along the inertial frame axes and define:

$$\phi_x = \tan^{-1}\left(\frac{\mathbf{p}_y}{\text{-}\mathbf{p}_z}\right), \; \phi_y = \text{-}\tan^{-1}\left(\frac{\mathbf{p}_x}{\text{-}\mathbf{p}_z}\right).$$

Fig. 1 pictures snapshots from an experiment. Fig. 6a-6b show Vicon measurements and estimated states during one trajectory period. For clarity, we plot only y components, however, performance in x is similar. At all cable lengths, the estimated state closely tracks the Vicon measurements.

Table II reports estimation errors. Let $\cdot_v$ denote Vicon measurements and $\cdot_e$ denote estimates. Angular errors are:

$$\frac{|\phi_{x,v} - \phi_{x,e}| + |\phi_{y,v} - \phi_{y,e}|}{2},$$

while $\dot{\mathbf{p}}$ errors are computed with:

$$\|\dot{\mathbf{p}}_v - \dot{\mathbf{p}}_e\|_2.$$

We observe an average orientation error of less than 2^o across all experiments, with a standard deviation of less than 1^o. Similarly, the average $\dot{\mathbf{p}}$ error is less than 0.11 1/s, with a standard deviation of less than 0.090 1/s in all experiments.

Fig. 8 illustrates tracking results for all experiments. Control gains were tuned with $l = 50$ cm; however, tracking performance remains consistent across all cable lengths. Errors in payload position and velocity control increase for faster trajectories, however, payload attitude tracking performance remains relatively constant.

C. Trajectory Tracking Through Slalom Course

Next, we execute trajectories through a slalom course of four equally spaced, collinear traffic cones, with $l = 50$ cm. The trajectory is constrained to pass through constant-altitude waypoints on alternating sides of the cones. We choose αs such that trajectory durations are $t_m = 1.5$ s, 1 s, 0.9 s (i.e. slow, medium, and fast, respectively). In all cases, the cable remains taut. From Eq. 11, all trajectories optimal with respect to Eq. 10 are piecewise-polynomials, making these experiments reflective of optimal slung-load maneuvers.

Fig. 9 illustrates desired payload trajectories with corresponding actual payload and quadrotor trajectories. Note the desired path is common across experiments, however, the payload angle significantly increases with trajectory speed. Table III lists the maximum payload velocities and angles. Notably, the payload reaches an angle of 53^o and over 3 m/s. Fig. 7 pictures snapshots from the fast trajectory.

Fig. 10 illustrates tracking and estimation performance along each trajectory. Estimation errors remain small across all trajectories, but tracking error increases for faster trajectories. In particular, $\mathbf{v}_{L,z}$ errors increase as it becomes difficult to keep the fast-moving payload at a constant altitude.

Table III also lists the percent reduction in average error of our proposed system compared to open-loop control [11]. We compare each slalom trajectory to a trajectory with comparable maximum payload velocity and angle optimized using the same QP formulation. While the compared trajectories are not identical, we can still gain an understanding of our proposed system's relative performance. We calculate error reduction as $\frac{\bar{e}_{open} - \bar{e}_{closed}}{\bar{e}_{open}}$, where $\bar{e}$ denotes the average error in payload position, $\|\mathbf{x}_{L,des} - \mathbf{x}_L\|_2$. In both the slow trajectory, where the payload remains close to the equilibrium position, and the fast trajectory, where the fast-moving payload becomes hard to track, over half the tracking error is eliminated.

Results in Sections VI-B-VI-C validate our system's capability to execute aggressive payload maneuvers at various cable lengths. We observe good performance in estimation across all experiments. The payload position tracking is better at low speeds. This is due to more drastic payload state changes in between successive camera measurements during fast trajectories. Further, as the desired payload higher-derivatives in

TABLE III: Statistics of slalom trajectories.

Speed	Max. $\|\dot{\mathbf{x}}_L\|_2$ (m/s)	Max. ϕ (deg)	Err. Reduction (%) (Open-Loop Max. $\|\dot{\mathbf{x}}_L\|_2, \phi$)
Slow	1.04	9.94	67 (1.05 m/s, 6.35^o)
Medium	2.14	32.88	61 (2.08 m/s, 32.00^o)
Fast	3.03	53.77	54 (2.87 m/s, 39.00^o)

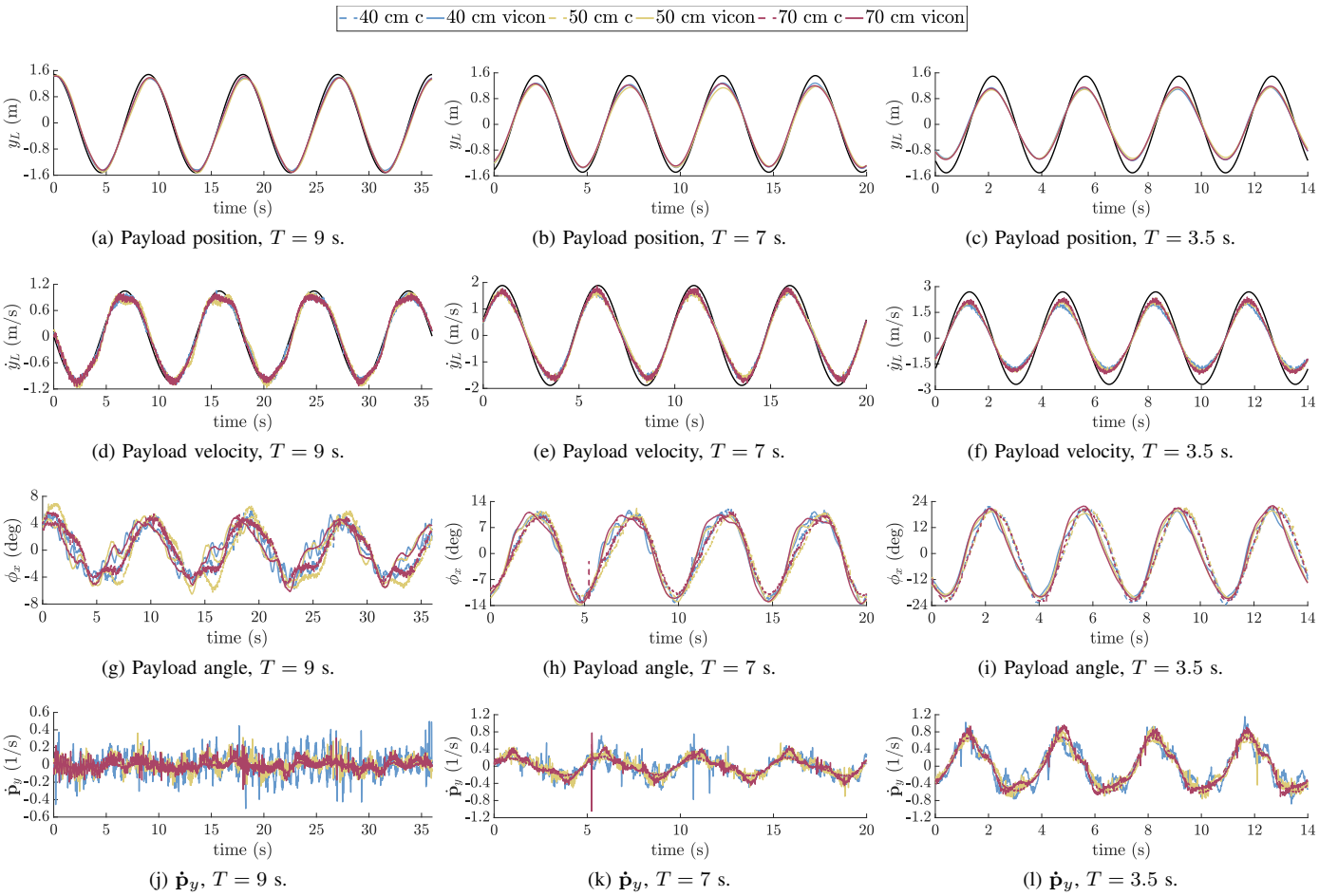

(a) Payload position, $T = 9$ s. (b) Payload position, $T = 7$ s. (c) Payload position, $T = 3.5$ s.

(d) Payload velocity, $T = 9$ s. (e) Payload velocity, $T = 7$ s. (f) Payload velocity, $T = 3.5$ s.

(g) Payload angle, $T = 9$ s. (h) Payload angle, $T = 7$ s. (i) Payload angle, $T = 3.5$ s.

(j) $\dot{\mathbf{p}}_y$, $T = 9$ s. (k) $\dot{\mathbf{p}}_y$, $T = 7$ s. (l) $\dot{\mathbf{p}}_y$, $T = 3.5$ s.

Fig. 8: Tracking of circle trajectories at various cable lengths and trajectory period times.

the controller's feedforward terms $\dot{\boldsymbol{R}}_c, \dot{\boldsymbol{\Omega}}_c, \dot{\mathbf{p}}_c$ increase, the system is more affected by unmodeled disturbances. However, even for fast trajectories, our system still demonstrates stable tracking and offers significant improvements over previous open-loop payload controllers. In short, we execute aggressive payload maneuvers using noisy, low-frequency visual feedback on a low-cost processor, representing a significant step towards real-world slung-load manipulation.

VII. Conclusions

In this work, we present a system for control, estimation, and trajectory generation of a quadrotor with a cable-suspended payload. With this method, we demonstrate closed-loop control of agile payload trajectories in the full three-dimensional workspace. We successfully execute our system on an onboard processor and demonstrate robust tracking of circular and piecewise-polynomial trajectories, while controlling payload angles of up to 53^o. The success of our approach suggests a natural direction for future work where vision-based state estimators for the quadrotor can be integrated with the proposed payload state estimator.

Acknowledgment

The authors would like to thank Jeremy Wang for the design and fabrication of our hardware components.

References

[1] J. Thomas, G. Loianno, J. Polin, K. Sreenath, and V. Kumar, "Toward autonomous avian-inspired grasping for micro aerial vehicles," *Bioinspiration & Biomimetics*, vol. 9, no. 2, p. 025010, Jun. 2014.

[2] M. Bernard and K. Kondak, "Generic slung load transportation system using small size helicopters," in *IEEE International Conference on Robotics and Automation (ICRA)*, 2009.

[3] M. Bisgaard, A. la Cour-Harbo, and J. D. Bendtsen, "Adaptive control system for autonomous helicopter slung load operations," *Control Engineering Practice*, vol. 18, no. 7, pp. 800 – 811, 2010, special Issue on Aerial Robotics.

[4] J. Potter, W. Singhose, and M. Costello, "Reducing swing of model helicopter sling load using input shaping," in *IEEE International Conference on Control and Automation (ICCA)*, Dec 2011, pp. 348–353.

[5] I. Palunko, R. Fierro, and P. Cruz, "Trajectory generation for swing-free maneuvers of a quadrotor with suspended payload: A dynamic programming approach," in *IEEE International Conference on Robotics and Automation (ICRA)*, May 2012, pp. 2691–2697.

[6] A. Faust, I. Palunko, P. Cruz, R. Fierro, and L. Tapia, "Automated aerial suspended cargo delivery through reinforcement learning," *Artificial Intelligence*, vol. 247, pp. 381–398, 2017, special Issue on {AI} and Robotics.

[7] P. O. Pereira, M. Herzog, and D. V. Dimarogonas, "Slung load transportation with a single aerial vehicle and disturbance removal," in *Mediterranean Conference on Control and Automation*, 2016, pp. 671–676.

[8] S. Tang and V. Kumar, "Mixed integer quadratic program trajectory generation for a quadrotor with a cable-suspended payload," in *2015 IEEE International Conference on Robotics and Automation (ICRA)*. Seattle: Institute of Electrical and Electronics Engineers (IEEE), May 26–30 2015, pp. 2215 – 22.

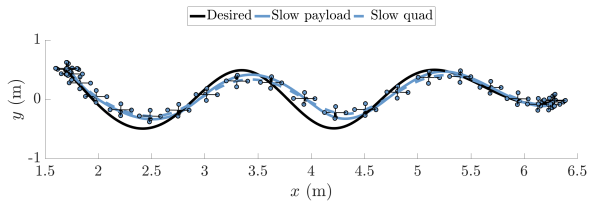

(a) Slow trajectory position.

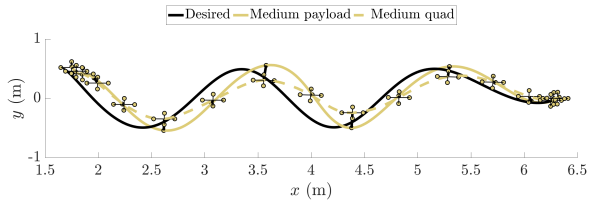

(b) Medium trajectory position.

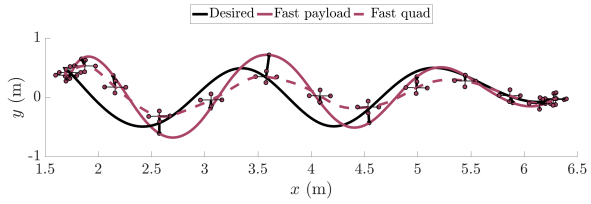

(c) Fast trajectory position.

Fig. 9: Waypoint trajectory for slalom avoidance.

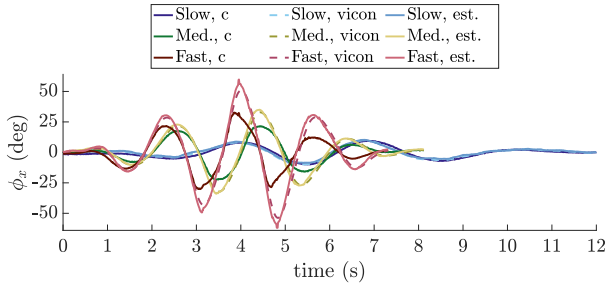

(a) Angle over time.

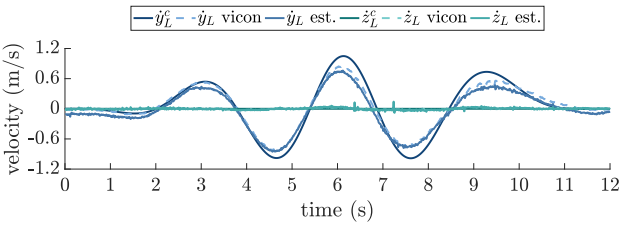

(b) Payload velocity for slow traversal.

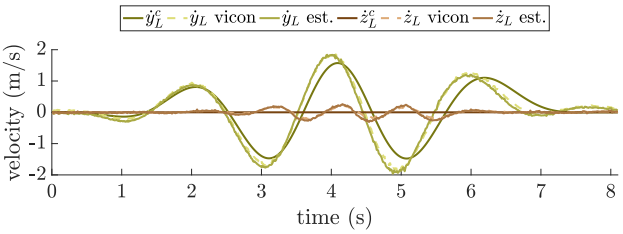

(c) Payload velocity for medium traversal.

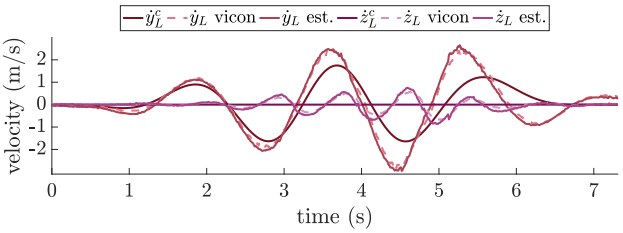

(d) Payload velocity for fast traversal.

Fig. 10: Tracking of waypoint trajectories at different speeds.

[9] C. de Crousaz, F. Farshidian, M. Neunert, and J. Buchli, "Unified motion control for dynamic quadrotor maneuvers demonstrated on slung load and rotor failure tasks," in *IEEE International Conference on Robotics and Automation (ICRA)*, May 2015, pp. 2223–2229.

[10] P. Foehn, D. Falanga, N. Kuppuswamy, R. Tedrake, and D. Scaramuzza, "Fast trajectory optimization for agile quadrotor maneuvers with a cable-suspended payload," in *Robotics: Science and Systems (RSS)*, Boston, July 12–16 2017.

[11] S. Tang, K. Sreenath, and V. Kumar, "Multi-robot trajectory generation for an aerial payload transport system," in *International Symposium on Robotics Research (ISRR)*, Dec. 2017.

[12] K. Sreenath, T. Lee, and V. Kumar, "Geometric control and differential flatness of a quadrotor UAV with a cable-suspended load," in *IEEE Conference on Decision and Control (CDC)*, Dec. 2013, pp. 2269–74.

[13] K. Sreenath, N. Michael, and V. Kumar, "Trajectory generation and control of a quadrotor with a cable-suspended load – a differentially-flat hybrid system," in *2013 IEEE International Conference on Robotics and Automation (ICRA)*. Karlsruhe: Institute of Electrical and Electronics Engineers (IEEE), May 6–10 2013, pp. 4888–95.

[14] F. Goodarzi, D. Lee, and T. Lee, "Geometric stabilization of a quadrotor uav with a payload connected by flexible cable," in *American Control Conference (ACC)*, June 2014, pp. 4925–4930.

[15] S. J. Lee and H. J. Kim, "Autonomous swing-angle estimation for stable slung-load flight of multi-rotor uavs," in *IEEE International Conference on Robotics and Automation (ICRA)*, May 2017, pp. 4576–4581.

[16] Y. Ling, T. Liu, and S. Shen, "Aggressive quadrotor flight using dense visual-inertial fusion," in *2016 IEEE International Conference on Robotics and Automation (ICRA)*. Stockholm: Institute of Electrical and Electronics Engineers (IEEE), May 16–21 2016, pp. 1499–1506.

[17] Y. Lin, F. Gao, T. Qin, W. Gao, T. Liu, W. Wu, Z. Yang, and S. Shen, "Autonomous aerial navigation using monocular visual-inertial fusion," *Journal of Field Robotics*, 2017.

[18] R. M. Murray, M. Rathinam, and W. Sluis, "Differential flatness of mechanical control systems: A catalog of prototype systems," in *ASME International Mechanical Engineering Congress and Exposition (IMECE)*. ASME, Nov. 1995.

[19] D. Mellinger and V. Kumar, "Minimum snap trajectory generation and control for quadrotors," in *Proceedings of the 2011 IEEE International Conference on Robotics and Automation (ICRA)*, Shanghai, China, May 2011, pp. 2520 – 2525.

[20] T. Lee, M. Leok, and N. H. McClamroch, "Nonlinear robust tracking control of a quadrotor UAV on SE(3)," in *2012 American Control Conference (ACC)*, Jun 2012, pp. 4649–4654.

[21] T. Krajník, M. Nitsche, J. Faigl, P. Vaněk, M. Saska, L. Přeučil, T. Duckett, and M. Mejail, "A practical multirobot localization system," *Journal of Intelligent & Robotic Systems*, 2014.

[22] D. Scaramuzza, A. Martinelli, and R. Siegwart, "A toolbox for easily calibrating omnidirectional cameras," in *Intelligent Robots and Systems, 2006 IEEE/RSJ International Conference on*. IEEE, 2006, pp. 5695–5701.

[23] S. Thrun, W. Burgard, and D. Fox, *Probabilistic Robotics (Intelligent Robotics and Autonomous Agents)*. The MIT Press, 2005.

[24] D. Scaramuzza, A. Martinelli, and R. Siegwart, "A flexible technique for accurate omnidirectional camera calibration and structure from motion," in *Computer Vision Systems, 2006 ICVS'06. IEEE International Conference on*. IEEE, 2006, pp. 45–45.